

Rational Pathways Tuning Facilitates Photoelectrochemical Upcycling of Nitrite to Ammonia Using CuPd Nanoalloy on GaN/Si Photocathode

Published as part of *Environmental Science & Technology* special issue “Materials Science and Environmental Applicability”.

Kejian Li,[§] Tianyin Qiu,[§] Bingxing Zhang, Zhengwei Ye, Jan Paul Menzel, Wan Jae Dong, Yuyang Pan, Songtao Tang, Zhuoran Long, Victor S. Batista,* and Zetian Mi*



Cite This: *Environ. Sci. Technol.* 2025, 59, 21715–21725



Read Online

ACCESS |



Metrics & More

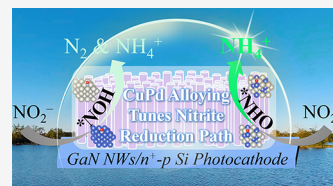


Article Recommendations



Supporting Information

ABSTRACT: Solar-driven photoelectrochemical conversion of nitrite to ammonia represents a sustainable yet unexplored approach for environmental remediation and resource recovery. Here, we demonstrate that Cu_5Pd_1 alloy nanoparticles, integrated with vertically grown GaN nanowires on an n⁺-p Si photocathode ($\text{Cu}_5\text{Pd}_1/\text{GaN}/\text{Si}$), enable highly efficient and selective nitrite reduction to ammonia. This photoelectrode achieves a Faradaic efficiency of 99.7% for NH_3 , with a yield rate of $162.2 \mu\text{mol h}^{-1} \text{cm}^{-2}$ and a nearly 100% selectivity. Additionally, the $\text{Cu}_5\text{Pd}_1/\text{GaN}/\text{Si}$ photoelectrode maintains robust performance in the presence of various anions and can effectively remove ~98% of nitrite even at low concentrations. Density functional theory calculations, supported by *in situ* spectroscopic techniques, reveal that Cu–Pd alloying fundamentally alters the nitrite reduction mechanisms. Unlike the *NOH-mediated pathway on Cu and Pd, which can lead to competing N_2 formation, the CuPd alloy preferentially stabilizes the *NHO intermediate, making NH_3 production thermodynamically preferred and highly selective. These findings highlight that a rational electrocatalyst design can effectively tune reaction pathways to enhance both the efficiency and selectivity of photoelectrocatalytic nitrite upcycling.



KEYWORDS: NO_2^- reduction, NH_3 synthesis, Photoelectrochemistry, CuPd alloy, Pathways tuning

INTRODUCTION

Overfertilization, industrial production, and fossil fuels consumption have released significant amounts of nitrate (NO_3^-) and nitrite (NO_2^-) into the environment, disturbing the global nitrogen cycle and posing serious risks to public health and the ecosystem.¹ NO_2^- , a key intermediate in NO_3^- reduction, has more serious adverse health effects such as the irreversible oxidation of hemoglobin and carcinogenic potential.² The WHO has classed NO_2^- as a 2A carcinogen, and the EPA strictly regulates NO_2^- concentration in drinking water to below 1 mg/L-N.^{3,4} Therefore, effective methods are urgently required to eliminate widespread nitrite in industrial wastewater, liquid nuclear waste, and surface water.

Owing to the low N–O bond dissociation energy and high solubility in aqueous solution compared to N_2 , electrocatalytic nitrite reduction is considered a “two birds with one stone” strategy for simultaneous environmental remediation and ammonia synthesis.^{5–7} Although driven by renewable energy, electrocatalysis generally operates effectively at high overpotentials,^{8,9} leading to extensive energy consumption and low energy efficiency. As an alternative, photoelectrocatalysis assisted by solar energy holds huge potentials in a wide range of reactions like water splitting,¹⁰ CO_2 reduction,¹¹

disinfectant production,¹² and biomass valorization,¹³ since the working biases can be largely reduced with the compensation of photoinduced voltages.^{14,15} To date, photoelectrocatalytic (PEC) nitrate reduction to ammonia has been investigated over various photoelectrodes,^{9,16–21} but the photocathode-based PEC nitrite conversion is rarely explored, particularly for the value-added ammonia synthesis.^{22,23} Compared to the eight-electron nitrate reduction with a high energy barrier of NO_3^- to NO_2^- , the short-step six-electron nitrite reduction is appealing for higher energy efficiency toward ammonia.⁸ Even though, the complex six-electron and eight-proton transfer process and the competing reactions (i.e., N_2 , NO , and H_2 formation) still challenge the efficiency and selectivity of NO_2^- -to- NH_3 conversion.^{24,25} In this context, developing a robust and selective photocathode for solar-driven nitrite-to-

Received: March 26, 2025

Revised: September 12, 2025

Accepted: September 17, 2025

Published: October 1, 2025



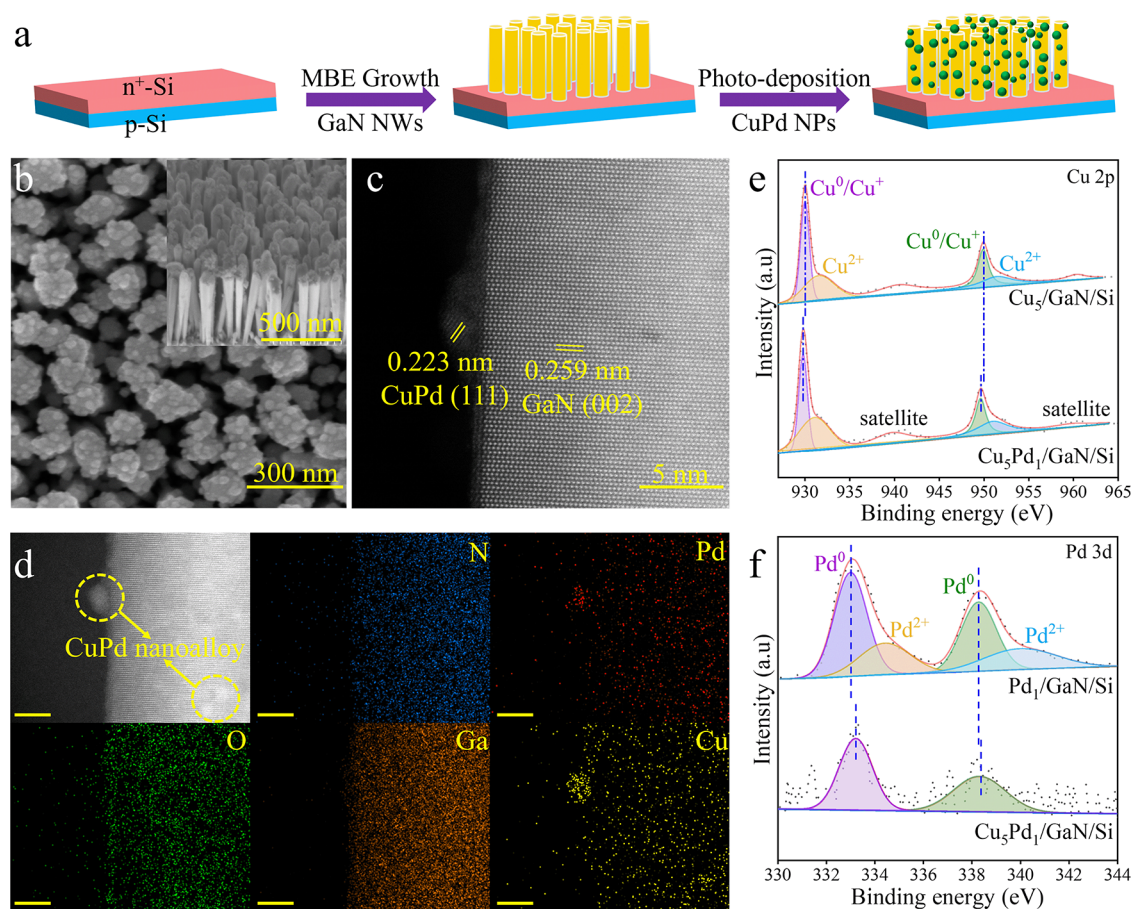


Figure 1. Characterizations of the prepared $\text{Cu}_5\text{Pd}_1/\text{GaN}/\text{Si}$ photocathode. (a) Schematic of the photoelectrode preparation processes. (b) Top and side view (inset) SEM images of the prepared $\text{Cu}_5\text{Pd}_1/\text{GaN}/\text{Si}$ photoelectrode. (c) HRTEM image and (d) EDS elemental mapping of CuPd nanoalloy decorated GaN nanowires. The scale bar in (d) is 5 nm. High-resolution XPS spectra of (e) Cu 2p and (f) Pd 3d recorded from different photoelectrodes, where the black scattered points are the experimental data, and the colorful lines represent fitting data.

ammonia conversion with favorable thermodynamics would offer both environmental and energy advantages.

Si, a low-cost and earth-abundant material, has been widely explored in photoelectrocatalysis and photovoltaics for solar energy conversion, due to its suitable band gap, strong visible light absorption, and mature fabrication infrastructure.²⁶ However, the bare Si photocathodes are not stable in aqueous solution and are of sluggish chemical activity, requiring electrocatalyst (also acts as protection layer) to improve charge carrier transfer, lower overpotential, and enhance reaction rates and stability.²⁷ One-dimensional GaN nanowires (NWs), a member of epitaxial III-nitride semiconductors, have attracted significant attention for applications in photo-(electro)catalysis and photoelectric devices, benefiting from tunable optoelectronic properties, chemical stability of a N-rich surface, and high electron mobility.^{28,29} Importantly, owing to the near-perfect alignment for the conduction band edge between GaN and Si, GaN has been demonstrated highly appropriate for forming GaN/Si heterojunction photocathode, leading to efficient electron transfer across the heterointerface and the significant stability improvement.³⁰ In addition, the vertically aligned GaN NWs can improve light absorption by reducing Fresnel reflection and promote catalytic reaction via providing high surface area for cocatalyst loading, as successfully demonstrated in PEC water splitting, CO_2 reduction, and urea synthesis.^{31–33} Moreover, our previous studies have revealed that GaN nanowires (NWs) exhibit

excellent ability for water dissociation under photoelectrochemical conditions, which is often challenging for conventional transition metal catalysts.^{11,27,32} This intrinsic capacity of GaN NWs may supply sufficient protons for photoelectrochemical nitrite reduction to ammonia through proton-coupled electron transfer processes (deoxygenation and hydrogenation).^{17,34} Even though, the reaction kinetics on pristine GaN NWs remain sluggish without cocatalysts. Metallic Pd is known for its extraordinary hydrogen adsorption capability,^{35–37} but it usually benefits N_2 generation with low selectivity toward NH_3 .^{38,39} In spite of this, the high resistance against poisoning and deactivation of Pd by intermediates makes it still promising for nitrogen oxyanions purification.⁴⁰ Optimizing electronic structures of Pd-based catalysts may adjust intermediate adsorption and tune reduction pathways to achieve selective ammonia synthesis. Cu has attracted significant attention as a cost-effective catalyst for nitrate/nitrite conversion with reasonable Faradaic efficiency to ammonia under high overpotentials.^{25,41,42} Thus, developing a robust CuPd nanoalloy cocatalyst that integrates with GaN NWs grown on a Si photocathode may enable selective and efficient PEC nitrite reduction to ammonia at low overpotentials.

In this study, we investigated photoelectrochemical nitrite reduction (PEC NO_2RR) using CuPd alloy nanoparticles on GaN nanowires grown on an n^+ -p Si photocathode. The optimized $\text{Cu}_5\text{Pd}_1/\text{GaN}/\text{Si}$ photoelectrode exhibited 99.7%

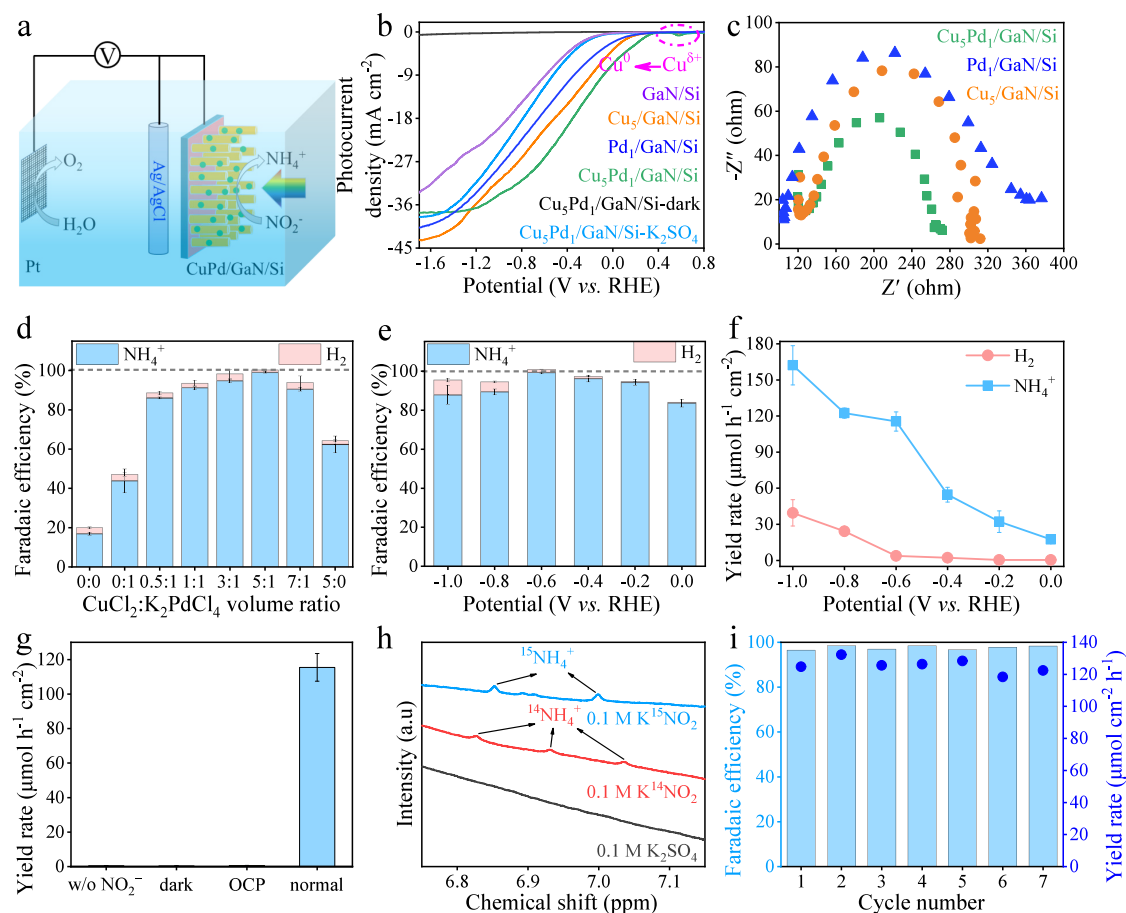


Figure 2. Photoelectrochemical NO_2^- reduction performance. (a) Schematic illustration of the three-electrode configuration for photoelectrochemical measurements. (b) LSV curves and (c) EIS spectra recorded for various photocathodes. (d) Faradaic efficiency of ammonia and hydrogen produced on the prepared photoelectrodes. (e) Potential-dependent Faradaic efficiency and (f) yield rate of NH_3 and H_2 on $\text{Cu}_5\text{Pd}_1/\text{GaN}/\text{Si}$ photocathode. (g) NH_3 yield rate during PEC reduction under different reaction conditions. (h) ^1H NMR spectra of electrolyte after PEC reaction using 0.1 M K_2SO_4 , K^{14}NO_2 , or K^{15}NO_2 as the feedstock. (i) Faradaic efficiency and yield rate of NH_3 during consecutive cycling experiments. Error bars represent the standard deviations from three independent experiments.

Faradaic efficiency and near-unity selectivity toward NH_3 with a high yield rate of $162.2 \mu\text{mol h}^{-1} \text{cm}^{-2}$. The influences of coexisting anions, electrolyte pH, and NO_2^- purification efficiency were investigated. A combination of *in situ* attenuated total reflectance Fourier-transform infrared (ATR-FTIR) spectroscopy and theoretical calculations revealed that a favorable $^*\text{NHO}$ -mediated pathway occurred on the CuPd nanoalloy rather than the $^*\text{NOH}$ -mediated paths on Cu and Pd, thus leading to highly efficient and selective nitrite upcycling.

MATERIALS AND METHODS

CuPd Nanoalloy Preparation. Co-catalyst CuPd alloy nanoparticles were synthesized on a prepared GaN/Si wafer using a photodeposition method. Specifically, the GaN/Si wafer was fixed on a Teflon holder and placed into a reaction chamber containing 60 mL of deionized water and 10 mL of methanol (Figure S1). Then 10 μL of 0.01 M K_2PdCl_4 and varying amounts ($x \mu\text{L}$, $x = 0, 0.5, 1, 3, 5$, and 7) of 0.1 M CuCl_2 were added, followed by vacuumizing for 3 min using a rotary pump. Subsequently, the GaN/Si wafer was irradiated with a Xe lamp (Cermox, PE300BU) for 30 min and the sample was thoroughly rinsed with deionized water. For the preparation of the Cu-loaded GaN/Si photoelectrode, the same procedure was followed except that only 5 μL of 0.1 M

CuCl_2 was added. The resulting samples were labeled as $\text{Cu}_x\text{Pd}_1/\text{GaN}/\text{Si}$, $\text{Cu}_5/\text{GaN}/\text{Si}$, and $\text{Pd}_1/\text{GaN}/\text{Si}$, respectively. Details on GaN/Si wafer fabrication and characterizations are provided in the Supporting Information.

Photoelectrochemical Measurements. Photoelectrochemical experiments were performed using a three-electrode configuration in an H-type electrolysis cell, separated by a Nafion 117 proton exchange membrane. The as-prepared GaN/Si-based photocathodes served as the working electrode, with a Pt wire and a Ag/AgCl electrode as the counter and reference electrodes, respectively. All applied potentials were converted against reverse hydrogen electrode (V_{RHE}) using the Nernst equation: $V_{\text{RHE}} = V_{\text{Ag/AgCl}} + 0.197 + 0.059 \times \text{pH}$. Linear sweep voltammetry (LSV) was conducted at a scan rate of 50 mV/s over the potential range from 0.8 to $-1.8 V_{\text{RHE}}$. Electrochemical impedance spectroscopy (EIS) was performed at $-0.6 V_{\text{RHE}}$ under light irradiation, across a frequency range of 0.01 to 10^5 Hz. Unless stated otherwise, the catholyte and anolyte were 0.1 M KNO_2 and 0.1 M K_2SO_4 , respectively, and the PEC NO_2RR was carried out by using chronoamperometry for 1 h. Light irradiation with 100 mW cm^{-2} was provided by an LCS-100 (ORIEL) solar simulator. Details on product analysis and the calculation formulas for Faradaic efficiency and yield rate are provided in Supporting Information.

DFT Calculations. Mechanistic studies are carried out using DFT calculations, and the computational details are shown in [Supporting Information](#).

RESULTS AND DISCUSSION

Characterizations of CuPd/GaN/Si Photocathode. The pristine GaN/Si wafer was fabricated using the molecular beam epitaxy (MBE) growth method. Co-catalyst Cu_xPd_1 nanoalloys were loaded via photodeposition (illustrated in [Figure 1a](#)). In the XRD pattern ([Figure S2](#)), the two prominent peaks at $\sim 32.9^\circ$ and $\sim 34.7^\circ$ were assigned to the (100) and (002) planes of wurtzite GaN nanowires, respectively.^{33,43} The dominant (002) reflection suggests preferential *c*-axis-oriented growth of the GaN NWs. No discernible diffraction peaks corresponding to CuPd alloy were observed, likely due to the low loading, small size, and high dispersion on the GaN surface. Micromorphology of the electrodes was examined using SEM. The prepared GaN/Si exhibited vertically grown, smooth GaN NWs with average lengths and diameters of 400 and 40 nm ([Figure S3](#)), respectively. Upon cocatalyst decoration (e.g., $\text{Cu}_5\text{Pd}_1/\text{GaN/Si}$), nanoparticles were deposited on the surface of GaN NWs, and the size of the supported nanoparticles mainly distributed in the range of 6–13 nm with an average value of ~ 9 nm ([Figures 1b, S4, and S5](#)). As shown in [Figure 1c](#), the HRTEM image further confirmed the successful loading of nanoalloys, and the lattice fringes with *d*-spacing of 0.259 and 0.223 nm were observed, corresponding to the GaN (002) plane and the (111) crystal facet of CuPd nanoalloy, respectively.^{31,44} Energy-dispersive X-ray spectroscopy ([Figure 1d](#)) revealed the homogeneous distribution of Cu, Pd, Ga, N, and O, with the overlapping distribution of Cu and Pd verifying the formation of a CuPd nanoalloy. In addition, the EDS analysis indicated the atomic ratio of Cu to Pd was about 10:1. The existence of oxygen is likely due to the unavoidable oxidation from exposure to ambient environment.⁴⁵

High-resolution X-ray photoelectron spectroscopy (XPS) was collected to investigate the surface chemical states of the photoelectrodes. As shown in [Figure S6](#), the XPS spectra of Ga 2p, N 1s, and O 1s remained nearly unchanged before and after the deposition of Cu_5Pd_1 alloy nanoparticles, indicating that the chemical states of GaN nanowires were minimally affected by surface metal decoration (Detailed peak fitting and analyses are provided in the [Supporting Information](#)). In high-resolution Cu 2p XPS spectra from the $\text{Cu}_5/\text{GaN/Si}$ photoelectrode ([Figure 1e](#)), peaks at 930.0 and 949.9 eV correspond to $\text{Cu}^0/\text{Cu}^+ 2p_{3/2}$ and $\text{Cu}^0/\text{Cu}^+ 2p_{1/2}$, while peaks at 931.3 and 951.2 eV are attributed to $\text{Cu}^{2+} 2p_{3/2}$ and $\text{Cu}^{2+} 2p_{1/2}$, respectively. Additionally, the peaks observed at approximately 940 and 960 eV were assigned to the satellite features of Cu $2p_{3/2}$ and Cu $2p_{1/2}$, respectively.^{18,46} Pd 3d XPS spectra ([Figure 1f](#)) from $\text{Pd}_1/\text{GaN/Si}$ show peaks corresponding to $\text{Pd}^0 3d_{5/2}$, $\text{Pd}^{2+} 3d_{5/2}$, $\text{Pd}^0 3d_{3/2}$, and $\text{Pd}^{2+} 3d_{3/2}$, located at approximately 333.0, 334.5, 338.3, and 340.2 eV, respectively.⁴⁷ The existence of oxidation state of Cu and Pd suggests the partial oxidation of samples exposed to air.⁴⁸ Notably, after Cu–Pd alloying, the Cu 2p peaks shifted to lower values while the Pd 3d peaks shifted toward higher binding energies, consistent with previous studies on CuPd nanoalloys.^{49,50} The binding-energy shifts indicate the existence of charge transfer between Pd and Cu and the alternations in their electronic structures upon alloy formation,⁵¹ which may lead to synergistic effects on

photoelectrocatalytic NO_2^- reduction. Although the Pd 3d signal intensity in CuPd nanoalloys was weaker than that from the $\text{Pd}_1/\text{GaN/Si}$ photoelectrode likely due to the competing photoreduction between Cu^{2+} and PdCl_4^{2-} , the successful formation of CuPd nanoalloys was supported by the EDS elemental mapping. Moreover, the characteristic peaks assigned to palladium oxides disappeared after alloying with Cu, possibly owing to the higher oxidation tendency of Cu compared to Pd.

Photoelectrochemical Performance of Nitrite Reduction. As illustrated in [Figure 2a](#), PEC NO_2RR was carried out under ambient conditions in a three-electrode configuration within an H-type electrolysis cell under simulated solar light irradiation. The LSV curves ([Figure 2b](#)) show that little to no current was observed in the dark, confirming that the chemical reaction was primarily driven by solar energy. Under light illumination, the photocurrent density measured on the $\text{Cu}_5\text{Pd}_1/\text{GaN/Si}$ photocathode at $-0.6 V_{\text{RHE}}$ decreased from -7.9 to -30.9 mA cm^{-2} and the onset potential (V_{onset} defined as at which the current density is -1 mA cm^{-2}) shifted from 0.04 to $0.29 V_{\text{RHE}}$, when 0.1 M KNO_2 was used in place of 0.1 M K_2SO_4 in the cathodic compartment. The results suggest the preferential and rapid nitrite reduction occurred on the developed photoelectrode. Besides, in the presence of 0.1 M KNO_2 , the photocurrent density at $-0.6 V_{\text{RHE}}$ followed the order of $\text{Cu}_5\text{Pd}_1/\text{GaN/Si} > \text{Cu}_5/\text{GaN/Si} > \text{Pd}_1/\text{GaN/Si} > \text{GaN/Si}$, with the V_{onset} values being approximately 0.29, 0.16, 0.05, and $-0.46 V_{\text{RHE}}$, respectively. Importantly, the photocurrent density and V_{onset} on the $\text{Cu}_5\text{Pd}_1/\text{Si}$ photocathode were significantly lower than those with GaN NWs, implying that the GaN NWs vertically grown on n^+p Si play a crucial role in enhancing electron transfer and facilitating NO_2^- conversion.⁵² A reduction peak at $\sim 0.3 V_{\text{RHE}}$ was observed in LSV curves of Cu-containing photoelectrodes, likely due to the reduction of $\text{Cu}^{\delta+}$ to Cu^0 .^{41,53} To further understand the charge transfer kinetics at the photoelectrode–electrolyte interface, EIS spectra were measured in the presence of nitrite and light irradiation. Typically, the radius of the semicircle in a Nyquist plot positively correlates with the interfacial charge transfer resistance.⁵⁴ As shown in [Figure 2c](#), the radius decreased in the following order: $\text{Pd}_1/\text{GaN/Si} > \text{Cu}_5/\text{GaN/Si} > \text{Cu}_5\text{Pd}_1/\text{GaN/Si}$, which inversely aligns with the trends in photocurrent density and indicates the faster surface reaction on the Cu_5Pd_1 nanoalloy. These measurements suggest that alloying Pd and Cu on GaN NWs shows huge potentials in PEC NO_2^- reduction compared with single-component Cu or Pd.

Photoelectrocatalytic activities on NO_2^- reduction to NH_3 were evaluated by chronoamperometry, and indophenol blue spectrophotometry was used to detect NH_3 production. As shown in [Figure 2d](#), at a constant potential of $-0.6 V_{\text{RHE}}$, the Faradaic efficiency to ammonia (FE_{NH_3}) on the bare GaN/Si photoelectrode was only about 16.9%, with a yield rate of $4.5 \mu\text{mol h}^{-1} \text{ cm}^{-2}$. The introduction of Cu and Pd nanoparticles improved FE_{NH_3} to 64.2% (yield rate, $21.9 \mu\text{mol h}^{-1} \text{ cm}^{-2}$) and 43.8% (yield rate, $19.6 \mu\text{mol h}^{-1} \text{ cm}^{-2}$), respectively. Significantly, the deposition of CuPd alloy nanoparticles greatly enhanced both the Faradaic efficiency and the yield rate for NH_3 production. Specifically, the FE_{NH_3} values of 86.1%, 91.2%, 94.8%, 99.7%, and 93.5% were achieved on $\text{Cu}_0.5\text{Pd}_1$, Cu_1Pd_1 , Cu_3Pd_1 , Cu_5Pd_1 , and $\text{Cu}_7\text{Pd}_1/\text{GaN/Si}$ photoelectrode, respectively, with the corresponding yield rate of 53.3, 85.8, 98.9, 115.5, and $102.2 \mu\text{mol h}^{-1} \text{ cm}^{-2}$. Hardly

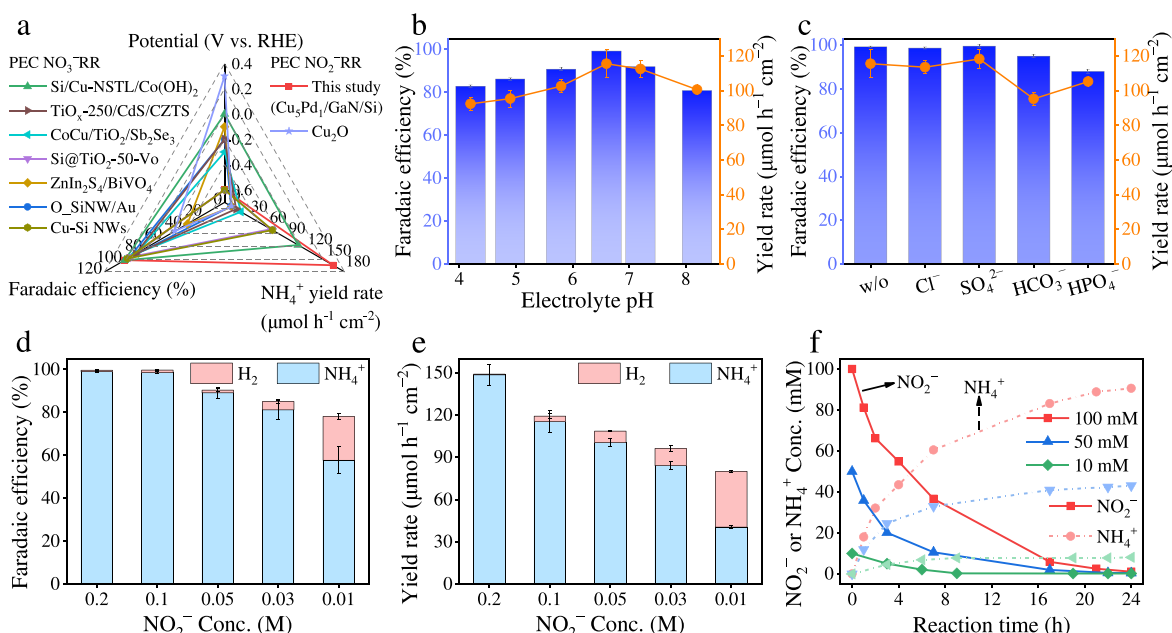


Figure 3. Effects of environmental factors on PEC NO₂RR. (a) Performance comparisons with recent studies on photoelectrocatalysis nitrate and nitrite reduction to ammonia. (b) Effects of electrolyte pH and (c) coexisting anions on the Faradaic efficiency of NH₃ production. NO₂⁻ concentration: 0.1 M. (d) Faradaic efficiency and (e) yield rate of NH₃ and H₂ in PEC NO₂RR at different NO₂⁻ concentrations. (f) Variations of NO₂⁻ concentration and NH₃ production during long-time experiments, where the colored solid lines are the concentrations of NO₂⁻ and the colored dash lines represent the production of NH₄⁺. Error bars represent the standard deviation from three independent experiments.

any byproduct like N₂H₄ was derived from PEC NO₂RR on Cu₅Pd₁ alloy nanoparticles (Figure S7), indicative of the near-unity selectivity to NH₃. In contrast, the Cu₅Pd₁/Si photocathode exhibited inferior performance (FE_{NH₃}, 65.2%; Yield rate, 43.2 μmol h⁻¹ cm⁻²; Figure S8), highlighting the crucial roles of CuPd alloy nanoparticles deposited on GaN nanowires, which provide synergistic effects for efficient and selective PEC NH₃ synthesis from NO₂⁻ conversion. Furthermore, as shown in Figures 2e and 2f, the Cu₅Pd₁/GaN/Si photoelectrode exhibited remarkable FE_{NH₃} (>95%) in a wide overpotential range from -0.2 to -0.8 V_{RHE} and the highest NH₃ yield rate of 162.2 μmol h⁻¹ cm⁻² was observed at -1.0 V_{RHE}. The insufficient nitrite conversion at comparatively positive voltages might be due to the accumulation of reduction intermediates on the electrode surface and the slow proton supply, while the decline at higher potentials is likely due to the enhanced HER and the limited mass transport.^{55,56}

Figure 2g shows that almost no NH₃ was detected after 1 h of reaction at open circuit potential (OCP), under dark condition at -0.6 V_{RHE}, or without NO₂⁻ under typical experimental conditions. The results rule out nitrogen contamination from the electrolytic cell or electrolyte, confirming that NH₃ was generated from NO₂⁻ reduction via the photoelectrocatalysis process. The isotope labeling experiments further verified that ammonia was synthesized from nitrite. As displayed in Figure 2h, a triple coupling peak corresponding to ¹⁴NH₄⁺ and a double peak attributable to ¹⁵NH₄⁺ were clearly detected in the ¹H NMR spectra of catholyte after photoelectrocatalysis, when 0.1 M of KNO₂ or K¹⁵NO₂ was used as nitrogen source, respectively.⁵⁷ Meanwhile, no peak was measured when 0.1 M K₂SO₄ was used as the catholyte, further confirming that the ammonia was formed from nitrite conversion. The stability of the Cu₅Pd₁/GaN/Si photoelectrode for PEC NO₂RR was evaluated through

performing consecutive cycling experiments. Figure 2i shows that the Faradaic efficiency and yield rate of NH₃ remained consistent across seven cycles, with the photocurrent density nearly identical in each cycle (Figure S9). Additionally, postreaction material characterizations were carried out after a 1-h photoelectrochemical nitrite reduction experiment. As shown in Figures S10 and S11, the crystal structure, morphology, and surface chemical states of the photoelectrode were insignificantly changed after chemical reaction, which suggested the high chemical and structural stability of the GaN/Si-based photoelectrode under reductive photoelectrochemical conditions. Note that there are currently very few studies focused on PEC nitrite reduction while PEC nitrate reduction has been extensively investigated, highlighting the significance of this frontier research on solar energy-powered nitrite conversion.^{9,16,21–23} As shown in Figure 3a and Table S1, the yield rate and Faradaic efficiency toward ammonia in previous PEC nitrite and nitrate reduction studies were generally lower than the values in this study using the Cu₅Pd₁/GaN/Si photoelectrode. These results highlight the importance of photoelectrocatalysis technology in green NH₃ synthesis from waste nitrogen-containing sources.

Effect of Environmental Factors. To assess the adaptivity of the Cu₅Pd₁/GaN/Si photocathode in real-world water matrices, the influences of environmental factors such as coexisting substances, electrolyte pH, and irradiation intensity were investigated. As shown in Figure 3b, a volcano relationship between FE_{NH₃} and the initial electrolyte pH was observed, with the initial neutral pH being optimal for PEC NO₂RR in NH₃ synthesis. Acidic conditions promoted adsorption of H⁺ on the photocathode, enhancing HER, while alkaline electrolyte suppressed proton availability, hindering the hydrogenation process.^{56,58} Figure 3c indicates that the addition of K₂SO₄ and KCl with a concentration of 10 mM had a negligible impact on the Faradaic efficiency to NH₃, while

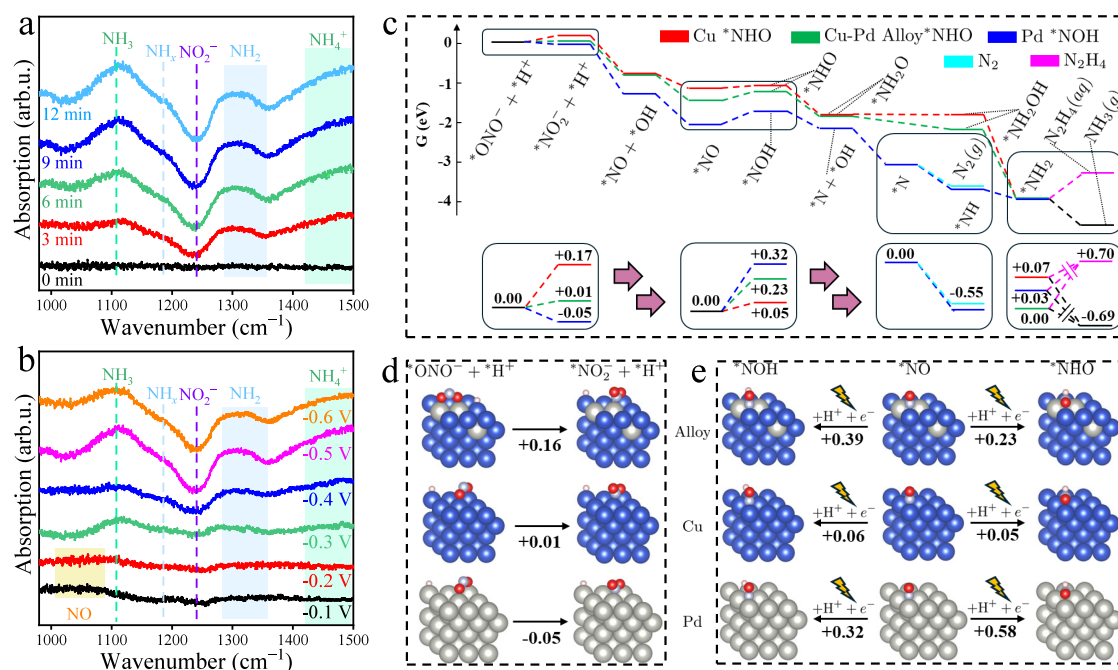


Figure 4. Mechanisms investigation of PEC NO_2^- reduction to NH_3 . (a) and (b) *In situ* ATR-FTIR spectra recorded at different reaction stages and under various potentials, respectively. (c) Free energy profile including only key steps for the reduction of nitrite to ammonia on Cu, CuPd alloy, and Pd metal surfaces, showing (from left to right) the initial conformational flip of nitrite on the metal surfaces, the possible routes for all metal surfaces (Cu can have both *NHO and *NOH routes, while only one possible route is preferred in CuPd and Pd), the N_2 side reaction, and the product formation step. (d) DFT-optimized structures of the reaction that flips *ONO to *NO_2 conformation on all three metal surfaces, reaction equation, and free energy differences (ΔG , in eV) for each step. (e) DFT-optimized structures of the selective reduction of *NO on all three metal surfaces, reaction equations, and free energy differences (ΔG , in eV) for each step.

KHCO_3 and KHPO_4 obviously reduced the FE_{NH_3} , probably due to the resulting increase in electrolyte pH (Figure S12). In addition, the maximum photocurrent density, dependent on the amount of charge carriers, is inherently controlled by light irradiation intensity (Figure S13a),⁵⁹ which may influence the efficiency of PEC NO_2RR . Figure S14a shows that the FE_{NH_3} maintained over 98% under the investigated irradiation intensity from 50 to 320 mW cm^{-2} . However, the NH_3 yield rate, as well as the recorded photocurrent density at $-0.6 \text{ V}_{\text{RHE}}$, was first increased and then declined with strengthening light illumination (Figures S13b and S14b). The highest ammonia production of $213.1 \mu\text{mol h}^{-1} \text{ cm}^{-2}$ was observed under 1.6 suns irradiation (160 mW cm^{-2}). The decreased performance was likely due to the limited mass transfer of nitrite, as supported by the gradually enhanced HER under stronger light irradiation. This issue can be addressed with the development and utilization of a flow-cell reactor, even under concentrated sunlight irradiation (tens to hundreds of suns),⁶⁰ which is currently being studied. Overall, these results demonstrate the robustness of the $\text{Cu}_3\text{Pd}_1/\text{GaN}/\text{Si}$ photocathode for NO_2^- reduction in real-world environments.

Nitrite Purification Efficiency. The impact of the nitrite concentration on the PEC NO_2RR was investigated using initial concentrations of 0.01, 0.03, 0.05, 0.1, and 0.2 M at a potential of $-0.6 \text{ V}_{\text{RHE}}$. As shown in Figures 3d and 3e, as the initial NO_2^- concentration decreased, both the Faradaic efficiency and yield rate of NH_3 dropped, while the Faradaic efficiency and production of H_2 increased. The results suggest that the higher NO_2^- concentrations favor ammonia production due to more effective mass transfer and reactant availability.^{61,62} To address the issue of low NO_2^- concentrations in wastewater, groundwater, and surface water, solar

energy-driven water evaporation to concentrate NO_2^- prior to photoelectrochemical reduction can be a potential strategy for simultaneous pollution treatment, NH_3 synthesis, and clean water production.^{63,64} Furthermore, NO_2^- purification using this photoelectrocatalysis technology was investigated in long-time experiments at a constant potential of $-0.6 \text{ V}_{\text{RHE}}$. Figure 3f depicted that the NO_2^- concentration steadily decreased over time, with elimination efficiencies exceeding 98% after 7, 20, and 24 h for initial NO_2^- concentrations of 0.01, 0.05, and 0.1 M, respectively. Meanwhile, both the photocurrent densities and FE_{NH_3} gradually declined over time due to the decrease on NO_2^- concentrations and increase in hydrogen evolution reaction (Figures S15 and S16). Notably, as shown in Figure S17, the higher the nitrite concentration, the higher the nitrogen balance during PEC reduction, and the nitrogen balance was reduced with reaction time increasing. The results further suggest that the high-concentration nitrite is beneficial to efficiently accept electrons for selective ammonia synthesis. The *in situ* ATR-FTIR experiments indicated the generation of the NO intermediate during nitrite reduction (*vide infra*), and some other byproducts and intermediates (e.g., NO and N_2O) might also be generated, particularly under a low-concentration environment. The formation of the undetected nitrogen-containing species may partially account for the observed nitrogen loss. In addition, the electrolyte pH was monitored during long-time PEC nitrite reduction with an initial nitrite concentration of 0.1 M. As shown in Figure S18, the pH values were increased to over 11 due to the consumption of protons for the hydrogenation reaction. The inevitable volatilization of NH_3 under alkaline conditions may contribute to the decrease in nitrogen balance during a prolonged reaction. Despite this, the results demonstrate that the sustainable and environ-

mental-friendly photoelectrocatalysis approach can effectively purify nitrite-containing wastewater while selectively converting the waste into valuable ammonia. Future optimization of the system by integrating a BiVO₄, WO₃, or Fe₂O₃-based photoanode would enable the bias-free utilization of both the reduction and oxidation reactions for environmental pollutants treatment and biomass-derived chemicals valorization, all driven by solar energy.^{18,65,66}

Mechanistic Investigation. To elucidate reaction mechanisms behind the efficient and selective PEC NO₂⁻ reduction to NH₃ on the Cu₅Pd₁/GaN/Si photoelectrode, *in situ* ATR-FTIR measurements were employed to detect intermediates during photoelectrocatalytic processes. Figure 4a shows time-dependent *in situ* ATR-FTIR spectra collected on a Cu₅Pd₁/GaN/Si photoelectrode in 0.2 M KNO₂ electrolyte at -0.5 V_{RHE}. As the reaction proceeded, a negative absorption band appeared at ~1240 cm⁻¹, assigned to the adsorbed *NO₂, and its intensity increased over time, indicating the occurrence of nitrite consumption and transformation through photoelectrochemical conversion.⁴ In the potential-dependent ATR-FTIR spectra (Figure 4b), the negative characteristic peak assigned to NO₂⁻ consumption appeared below -0.3 V_{RHE}, aligning with the enhanced PEC nitrite reduction at more negative overpotentials. Alongside NO₂⁻ consumption, several characteristic bands associated with reduction intermediates were observed, including *NO (~1040 cm⁻¹), *NH_x and *NH₂OH (1160–1210 cm⁻¹), and *NH₂ (1270–1340 cm⁻¹), confirming the occurrence of deoxygenation and hydrogenation of surface-bound *NO₂ species.^{67,68} The absorption signals of *NO were mainly detected at low overpotentials, likely because it is easy to reduce to generate NH_x species under a more negative potential. Importantly, the absorption bands of NH₃ and NH₄⁺ were detected at approximately 1108 and 1460 cm⁻¹, respectively, with peak intensities increasing as the reaction proceeded and under more negative biases. In contrast, as shown in Figure S19, the *in situ* ATR-FTIR spectra recorded from Cu₅/GaN/Si and Pd₁/GaN/Si photoelectrodes at -0.5 V_{RHE} showed weaker signals for *NH_x, *NH₂, and *NH₄⁺, indicating the low efficiency in nitrite-to-ammonia conversion on Cu and Pd nanoparticles. Thus, the *in situ* ATR-FTIR experiment confirmed that Cu₅Pd₁ nanoalloys on GaN NWs showed synergistic effects to enhance hydrogenation processes for efficient and selective reduction of nitrite to ammonia.

To further investigate the reaction pathways for nitrite reduction to ammonia, density functional theory (DFT) calculations were conducted on four cocatalysts: Pd, Cu, CuPd 2-site alloy, and CuPd 1-site alloy (Model structure shown in Figure S20). The catalyst models incorporating either one or two surface Pd atoms were referred to as CuPd 1-site alloy and CuPd 2-site alloy, respectively). This theoretical analysis aimed to explain differences in photoelectrocatalytic performance and synergistic effects within the nanoalloy. Figure 4c shows the relative free energies of nitrite reduction comparing the CuPd 2-site alloy with pure metal slabs, normalized to the initial *ONO intermediate. Although adsorption energies vary across different surfaces, normalization to the *ONO binding mode provides a consistent reference point. This normalization ensures that uniform shifts in adsorption strength do not affect the computed thermodynamic barriers, which form the basis for mechanistic comparisons. Importantly, the binding energies of nitrite on all examined metal surfaces are negative (Table S4),

confirming that adsorption remains thermodynamically favorable and does not hinder the overall reaction. The DFT-optimized structures and free energy changes for key steps are detailed in Figures 4d and 4e, as well as in Supporting Information. The photoelectrocatalytic nitrite reduction, which involves six-electron and eight-proton transfer, is thermodynamically favorable on all three metallic surfaces. The process begins with nitrite adsorption in two possible bidentate configurations: *ONO (both oxygen atoms interacting with the surface) or *NO₂ (one oxygen and one nitrogen interacting), and the two modes exist in equilibrium. Notably, the *NO₂ configuration is essential for N-O bond cleavage, forming *NO and *OH, making the process irreversible (Figure 4c). While *NO₂ adsorption is thermodynamically accessible on Pd and CuPd 2-site alloy, Cu uniquely favors the *ONO mode over *NO₂ (Figures 4c and 4d). This binding preference aligns with prior studies on electrochemical nitrate reduction on Cu, where nitrite was the main product due to the strong binding of NO₃⁻ and the limited accessibility of the *ONO intermediate, creating a thermodynamic barrier for further reduction progress.^{42,69} The preference for *ONO binding on Cu can also be rationalized using hard and soft acid and base theory: nitrogen, a softer Lewis base than oxygen, binds preferentially to the softer Pd, while the harder Lewis acid Cu favors oxygen binding over nitrogen.^{70,71} Additionally, such preference seems to happen at a site where at least two adjacent Pd atoms exists, as indicated by comparing such a barrier between the two-site alloy and one-site alloy calculation shown in Figures S21 and S22.

Following N-O bond dissociation, *NO and *OH form on the catalyst surface, after which hydroxide removal reduces the formally charged metal surface, leaving adsorbed *NO. At this stage, three reaction pathways are possible: (i) hydrogenation of nitrogen to form *NHO; (ii) hydrogenation of oxygen to form *NOH; and (iii) N-O bond dissociation to generate *N and *O. Route iii is thermodynamically unfavorable (Figure S23). Interestingly, the three metal surfaces exhibit distinct preferences for pathways i and ii (Figure 4e). Specifically, on Cu metal, the thermodynamic barriers for *NHO and *NOH are 0.05 and 0.06 eV, respectively, suggesting both pathways are accessible under reductive conditions. On metallic Pd, the thermodynamic barriers increase to 0.58 (*NHO) and 0.32 eV (*NOH), favoring *NOH formation. On both CuPd alloys, the trend reverses. On the CuPd two-site alloy, where the flipping of preference is more pronounced, *NHO formation requires 0.23 eV and *NOH requires 0.39 eV, indicating a shift in the reaction pathway during PEC NO₂RR due to the Cu-Pd alloying. It is noteworthy that, when applying a potential correction of -0.4 V using the computational hydrogen electrode (CHE) method by Nørskov et al.,⁷² all reduction steps of *NO became energetically favorable, except for the formation of *NHO on Pd (Figures S24 and S25). It is also interesting to see that under -0.4 V of potential correction all reduction steps of *NO became energetically favorable, with the exception of the *NHO forming step on Pd (Figures S24 and S25). All corrected energy barriers are also highly consistent with previous studies.^{73,74} Importantly, the *NHO-mediated pathways were also demonstrated favorable to electrocatalytic nitrate reduction to NH₃,^{75,76} which further supported the rational pathway tuning on CuPd nanoalloys contributing to the efficient and selective photoelectrochemical ammonia production in this study.

The pathway divergence may lead to different products, and such trends are consistent across the experimental observations and theoretical pathways. On all three surfaces, subsequent reactions after the crucial hydrogenation of *NO step that determines whether the reaction proceeds via pathways i or ii are energetically downhill from the theoretical calculations. However, the *NOH -mediated pathway ii can lead to undesirable N_2 formation via an *N radical intermediate, whereas the *NHO -dominated pathway i selectively produces ammonia. This trend is supported by the experimentally observed near-unity selectivity and $\sim 100\%$ Faradaic efficiency of Cu_3Pd_1 nanoalloy (Figure 2d), indicating that nitrite reduction predominantly follows pathway i on these alloy nanoparticles integrated with GaN NWs grown on n⁺-p Si (Figure S21). In contrast, Pd exhibits significantly lower Faradaic efficiency in experiments, which is consistent with the theoretically determined competition between ammonia formation and N_2 release due to the dominant *NOH pathway (Figure S26). The Cu surface shows intermediate efficiency in experiments, in agreement with the theoretical studies, as both *NHO and *NOH pathways are suggested to contribute equally due to their comparable thermodynamic barriers, leading to mixed ammonia and N_2 production (Figure S27). Note that entering the *NHO path does not categorically preclude N_2 formation; our mechanistic analysis shows that alternative decomposition pathways from *NHO —such as N–H or N–O bond cleavage—either regenerate intermediates like *NO or proceed toward *NH formation, which is more likely to yield NH_3 upon further reduction. The further dissociation of *NO is also proven unlikely, as suggested by Figure S23.

Furthermore, to experimentally validate the theoretical findings, NO_2^- consumption and NH_4^+ production on $Cu_5/GaN/Si$ and $Pd_1/GaN/Si$ were investigated at $-0.6 V_{RHE}$ for 1 h. Due to background interference, N_2 quantification was challenging, but the difference between reduced NO_2^- concentration and NH_4^+ production was significant, particularly for the $Pd_1/GaN/Si$ photoelectrode (Figure S28a). The negligible N_2H_4 detection (Figure S28b) as well as the uphill energy barrier of N_2H_4 formation from *NH_2 intermediate from DFT calculations (Figure 4c and Figures S26–S27) further confirms that the low NH_3 selectivity on $Cu_5/GaN/Si$ and $Pd_1/GaN/Si$ photocathodes was likely due to the generation of N_2 through the *NOH -mediated pathway and some other intermediates and byproducts. Thus, by combining experimental measurements and theoretical investigations, this study demonstrates that Cu–Pd alloying steers the photoelectrocatalytic nitrite reduction predominantly via the *NHO -mediated pathway, enabling selective NH_3 production.

ENVIRONMENTAL IMPLICATIONS

Nitrite, a common inorganic pollutant in industrial wastewater, agricultural runoff, groundwater, and surface water, poses significant threats to both aquatic life and human health due to its carcinogenic potential. Traditional treatment methods, such as ion exchange, reverse osmosis, and biological denitrification, are hindered by slow reaction kinetics and the risk of secondary pollution. Ammonia, an important chemical for fertilizer production and hydrogen storage, is currently produced by Haber-Bosch processes under high pressures and temperatures. Converting nitrite waste into valuable ammonia through photoelectrocatalysis is a sustainable “win-win” strategy for water purification and resource recovery. In this study, we demonstrate the efficient and selective

photoelectrochemical nitrite reduction to ammonia using a CuPd nanoalloy on an earth-abundant GaN/Si photocathode. This PEC system achieves Faradaic efficiency to ammonia over 95% across a wide potential range, with maximum ammonia yield rate of approximately $162.2 \mu mol h^{-1} cm^{-2}$ at $-1.0 V_{RHE}$. Besides, the PEC NO_2RR to NH_3 operates effectively in the presence of various coexisting anions and under different light irradiation intensities, simultaneously with NO_2^- removal efficiency higher than 98%. DFT theoretical calculations, in combination with *in situ* ATR-FTIR experiments, reveal the *NHO -mediated thermodynamically favorable pathways to selectively produce ammonia occurred on CuPd alloy nanoparticles, which differs from the *NOH -mediated mechanisms competitively generating N_2 on Cu and Pd nanoparticles. The findings indicate that rationally regulating nitrite reduction pathways via tuning the electronic structure and components of electrocatalysts is of great promise in nitrite reduction to ammonia. This direct solar-powered photoelectrochemical approach provides a sustainable alternative for decentralized ammonia production from nitrogen-containing pollutants with broad implications for waste upgrading and carbon neutrality.

ASSOCIATED CONTENT

Supporting Information

The Supporting Information is available free of charge at <https://pubs.acs.org/doi/10.1021/acs.est.5c04038>.

GaN/Si photocathode fabrication, catalyst characterization, product analytic methods, and DFT calculations (PDF)

AUTHOR INFORMATION

Corresponding Authors

Victor S. Batista – Department of Chemistry and Energy Sciences Institute, Yale University, New Haven, Connecticut 06520, United States; orcid.org/0000-0002-3262-1237; Email: victor.batista@yale.edu

Zetian Mi – Department of Electrical Engineering and Computer Science, University of Michigan, Ann Arbor, Michigan 48109, United States; orcid.org/0000-0001-9494-7390; Email: ztmi@umich.edu

Authors

Kejian Li – Department of Electrical Engineering and Computer Science, University of Michigan, Ann Arbor, Michigan 48109, United States; orcid.org/0009-0004-2356-4914

Tianyin Qiu – Department of Chemistry and Energy Sciences Institute, Yale University, New Haven, Connecticut 06520, United States

Bingxing Zhang – Department of Electrical Engineering and Computer Science, University of Michigan, Ann Arbor, Michigan 48109, United States

Zhengwei Ye – Department of Electrical Engineering and Computer Science, University of Michigan, Ann Arbor, Michigan 48109, United States

Jan Paul Menzel – Department of Chemistry and Energy Sciences Institute, Yale University, New Haven, Connecticut 06520, United States; orcid.org/0000-0002-1312-5000

Wan Jae Dong – Department of Electrical Engineering and Computer Science, University of Michigan, Ann Arbor, Michigan 48109, United States; orcid.org/0000-0002-8520-5587

Yuyang Pan – Department of Electrical Engineering and Computer Science, University of Michigan, Ann Arbor, Michigan 48109, United States

Songtao Tang – Department of Electrical Engineering and Computer Science, University of Michigan, Ann Arbor, Michigan 48109, United States

Zhuoran Long – Department of Chemistry and Energy Sciences Institute, Yale University, New Haven, Connecticut 06520, United States; orcid.org/0000-0002-2957-9568

Complete contact information is available at:
<https://pubs.acs.org/10.1021/acs.est.5c04038>

Author Contributions

[§](K.L., T.Q.) These authors contributed equally.

Notes

The authors declare the following competing financial interest(s): Some IP related to this work was licensed to NX Fuels, Inc., which was co-founded by Z. Mi. The University of Michigan and Mi have a financial interest in the company.

ACKNOWLEDGMENTS

The authors gratefully acknowledge research support from US Army Research Office under Award Number W911NF2110337 and from National Science Foundation under Award Number 2330525.

REFERENCES

- (1) Chen, R.; Wang, J.; Zhang, C.; Sun, Y.; Li, J.; Dong, F. Purification and value-added conversion of NO_x under ambient conditions with photo-/electrocatalysis technology. *Environ. Sci. Technol.* **2025**, *59* (2), 1013–1033.
- (2) Zhang, X.; Wang, Y.; Wang, Y.; Guo, Y.; Xie, X.; Yu, Y.; Zhang, B. Recent advances in electrocatalytic nitrite reduction. *Chem. Commun.* **2022**, *58* (17), 2777–2787.
- (3) Yan, C.; Kakuturu, S.; Butzlaff, A. H.; Cwiertny, D. M.; Mubeen, S.; Werth, C. J. Scalable reactor design for electrocatalytic nitrite reduction with minimal mass transfer limitations. *ACS ES&T Engg.* **2021**, *1* (2), 204–215.
- (4) Xiang, J.; Qiang, C.; Shang, S.; Chen, K.; Kang, C.; Chu, K. Tandem electrocatalytic reduction of nitrite to ammonia on rhodium-copper single atom alloys. *Adv. Funct. Mater.* **2024**, *34* (36), No. 2401941.
- (5) Zhang, J.; Zhao, B.; Liang, W.; Zhou, G.; Liang, Z.; Wang, Y.; Qu, J.; Sun, Y.; Jiang, L. Three-phase electrolysis by gold nanoparticle on hydrophobic interface for enhanced electrochemical nitrogen reduction reaction. *Adv. Sci.* **2020**, *7* (22), No. 2002630.
- (6) Wang, J. J.; Bui, H. T. D.; Wang, X.; Lv, Z.; Hu, H.; Kong, S.; Wang, Z.; Liu, L.; Chen, W.; Bi, H.; Yang, M.; Brinck, T.; Wang, J.; Huang, F. A copper-zinc cyanamide solid-solution catalyst with tailored surface electrostatic potentials promotes asymmetric N-intermediate adsorption in nitrite electroreduction. *J. Am. Chem. Soc.* **2025**, *147* (9), 8012–8023.
- (7) Mao, C.; Wang, J.; Zou, Y.; Shi, Y.; Viasus, C. J.; Loh, J. Y. Y.; Xia, M.; Ji, S.; Li, M.; Shang, H.; Ghossoub, M.; Xu, Y.-F.; Ye, J.; Li, Z.; Kherani, N. P.; Zheng, L.; Liu, Y.; Zhang, L.; Ozin, G. A. Photochemical acceleration of ammonia production by Pt₁-Pt_n-TiN reduction and N₂ activation. *J. Am. Chem. Soc.* **2023**, *145* (24), 13134–13146.
- (8) Zhang, Z.; Niu, A.; Lv, Y.; Guo, H.; Chen, J. S.; Liu, Q.; Dong, K.; Sun, X.; Li, T. NbC nanoparticles decorated carbon nanofibers as highly active and robust heterostructural electrocatalysts for ammonia synthesis. *Angew. Chem., Int. Ed.* **2024**, *63* (30), No. e202406441.
- (9) Li, Y.; Zhang, Q.; Dai, H.; He, D.; Ke, Z.; Xiao, X. Photoelectrochemical nitrate denitrification towards acidic ammonia synthesis on copper-decorated black silicon. *Energy Environ. Sci.* **2024**, *17* (23), 9233–9243.
- (10) Yang, W.; Prabhakar, R. R.; Tan, J.; Tilley, S. D.; Moon, J. Strategies for enhancing the photocurrent, photovoltage, and stability of photoelectrodes for photoelectrochemical water splitting. *Chem. Soc. Rev.* **2019**, *48* (19), 4979–5015.
- (11) Zhang, B.; Zhou, P.; Ye, Z.; Navid, I. A.; Pan, Y.; Xiao, Y.; Sun, K.; Mi, Z. Interfacially coupled Cu-cluster/GaN photocathode for efficient CO₂ to ethylene conversion. *Nat. Synthesis* **2024**, *3* (12), 1567–1576.
- (12) Gao, R.-T.; Gao, Z.; Nguyen, N. T.; Chen, J.; Liu, X.; Wang, L.; Wu, L. Photoelectrochemical production of disinfectants from seawater. *Nat. Sustain.* **2025**, *8* (6), 672–681.
- (13) Pan, Y.; Zhang, H.; Zhang, B.; Gong, F.; Feng, J.; Huang, H.; Vanka, S.; Fan, R.; Cao, Q.; Shen, M.; Li, Z.; Zou, Z.; Xiao, R.; Chu, S. Renewable formate from sunlight, biomass and carbon dioxide in a photoelectrochemical cell. *Nat. Commun.* **2023**, *14* (1), 1013.
- (14) Poonia, K.; Singh, P.; Singh, A.; Thakur, S.; Van Le, Q.; Ahamad, T.; Raizada, P.; Wang, C.; Nguyen, L. H.; Nguyen, V.-H. Photoelectrocatalytic systems for simultaneous energy recovery and wastewater treatment: a review. *Environ. Chem. Lett.* **2023**, *21* (1), 265–283.
- (15) Tian, Z.; Da, Y.; Wang, M.; Dou, X.; Cui, X.; Chen, J.; Jiang, R.; Xi, S.; Cui, B.; Luo, Y.; et al. Selective photoelectrochemical oxidation of glucose to glucaric acid by single atom Pt decorated defective TiO₂. *Nat. Commun.* **2023**, *14* (1), 142.
- (16) Ren, S.; Gao, R.; Nguyen, N. T.; Wang, L. Enhanced charge carrier dynamics on Sb₂Se₃ photocathodes for efficient photoelectrochemical nitrate reduction to ammonia. *Angew. Chem., Int. Ed.* **2024**, *63* (11), No. e202317414.
- (17) Silveira, V. R.; Bericat-Vadell, R.; Sá, J. Photoelectrocatalytic conversion of nitrates to ammonia: effect of proton donor. *ChemPhotoChem.* **2024**, *8* (8), No. e202300313.
- (18) Su, K.; Ren, S.; Gao, R.-T.; Bai, G.-E.; Wu, L.; Wang, L. Bias-free solar-driven ammonia coupled to C₃-dihydroxyacetone production through photoelectrochemistry. *Angew. Chem., Int. Ed.* **2025**, *64* (14), No. e202422443.
- (19) Kim, H. E.; Kim, J.; Ra, E. C.; Zhang, H.; Jang, Y. J.; Lee, J. S. Photoelectrochemical nitrate reduction to ammonia on ordered silicon nanowire array photocathodes. *Angew. Chem., Int. Ed.* **2022**, *61* (25), No. e202204117.
- (20) Wang, F.; Ding, Q.; Ding, J.; Bai, Y.; Bai, H.; Fan, W. Frustrated Lewis pairs boosting photoelectrochemical nitrate reduction over ZnIn₂S₄/BiVO₄ heterostructure. *Chem. Eng. J.* **2022**, *450*, No. 138260.
- (21) Han, C.; Li, C.; Yuwono, J. A.; Liu, Z.; Sun, K.; Wang, K.; He, G.; Huang, J.; Kumar, P. V.; Vongsvivut, J.; Cong, J.; Mehrvarz, H.; Han, Z.; Lu, X.; Pan, J.; Hao, X.; Amal, R. Nanostructured hybrid catalysts empower the artificial leaf for solar-driven ammonia production from nitrate. *Energy Environ. Sci.* **2024**, *17* (15), 5653–5665.
- (22) Kim, H. E.; Wi, D. H.; Lee, J. S.; Choi, K.-S. Photoelectrochemical nitrate and nitrite reduction using Cu₂O photocathodes. *ACS Energy Lett.* **2024**, *9* (5), 1993–1999.
- (23) Song, Y.; Wu, Y.; Cao, S.; Zhang, Y.; Luo, D.; Gao, J.; Li, Z.; Sun, L.; Hou, J. Simultaneous photoelectrocatalytic oxidation and nitrite-ammonia conversion with artificial photoelectrochemistry cells. *Adv. Energy Mater.* **2022**, *12* (48), No. 2201782.
- (24) Tong, J.; Tan, P.; Zhai, H.; Lu, K.; Lu, M.; Tang, Y. F.; Liu, M.; Liao, H.; Xie, J.; Pan, J. Enhancing localized electron density over Pd_{1.4}Cu decorated oxygen defective TiO_{2-x} nanoarray for electrocatalytic nitrite reduction to ammonia. *Small* **2024**, *20* (46), No. 2403865.
- (25) Lan, J.; Wang, Z.; Kao, C.-w.; Lu, Y.-R.; Xie, F.; Tan, Y. Isolating Cu-Zn active-sites in ordered intermetallics to enhance nitrite-to-ammonia electroreduction. *Nat. Commun.* **2024**, *15* (1), 10173.
- (26) Zhang, D.; Shi, J.; Zi, W.; Wang, P.; Liu, S. Recent advances in photoelectrochemical applications of silicon materials for solar-to-chemicals conversion. *ChemSusChem* **2017**, *10* (22), 4324–4341.
- (27) Zeng, G.; Pham, T. A.; Vanka, S.; Liu, G.; Song, C.; Cooper, J. K.; Mi, Z.; Ogitsu, T.; Toma, F. M. Development of a photo-

electrochemically self-improving Si/GaN photocathode for efficient and durable H₂ production. *Nat. Mater.* **2021**, *20* (8), 1130–1135.

(28) Zhou, B.; Zhou, P.; Dong, W.; Mi, Z. Gallium nitride-based artificial photosynthesis integrated devices for solar hydrogen generation and carbon dioxide reduction. *Conversion of Water and CO₂ to Fuels using Solar Energy* **2024**, 309–339.

(29) Dong, W. J.; Mi, Z. One-dimensional III-nitrides: towards ultrahigh efficiency, ultrahigh stability artificial photosynthesis. *J. Mater. Chem. A* **2023**, *11* (11), 5427–5459.

(30) Vanka, S.; Arca, E.; Cheng, S.; Sun, K.; Botton, G. A.; Teeter, G.; Mi, Z. High efficiency Si photocathode protected by multifunctional GaN nanostructures. *Nano Lett.* **2018**, *18* (10), 6530–6537.

(31) Dong, W. J.; Navid, I. A.; Xiao, Y.; Lim, J. W.; Lee, J. L.; Mi, Z. CuS-decorated GaN nanowires on silicon photocathodes for converting CO₂ mixture gas to HCOOH. *J. Am. Chem. Soc.* **2021**, *143* (27), 10099–10107.

(32) Xiao, Y.; Kong, X.; Vanka, S.; Dong, W. J.; Zeng, G.; Ye, Z.; Sun, K.; Navid, I. A.; Zhou, B.; Toma, F. M.; Guo, H.; Mi, Z. Oxynitrides enabled photoelectrochemical water splitting with over 3,000 h stable operation in practical two-electrode configuration. *Nat. Commun.* **2023**, *14* (1), 2047.

(33) Dong, W. J.; Menzel, J. P.; Ye, Z.; Navid, I. A.; Zhou, P.; Yang, K. R.; Batista, V. S.; Mi, Z. Photoelectrochemical urea synthesis from nitrate and carbon dioxide on GaN nanowires. *ACS Catal.* **2024**, *14* (4), 2588–2596.

(34) Xu, Y.; Cheng, C.; Zhu, J.; Zhang, B.; Wang, Y.; Yu, Y. Sulphur-boosted active hydrogen on copper for enhanced electrocatalytic nitrate-to-ammonia selectivity. *Angew. Chem., Int. Ed.* **2024**, *63* (16), No. e202400289.

(35) Li, K.; Yang, Y.; Bacha, A.-U.-R.; Feng, Y.; Ajmal, S.; Nabi, I.; Zhang, L. Efficiently complete degradation of 2, 4-DCP using sustainable photoelectrochemical reduction and sequential oxidation method. *Chem. Eng. J.* **2019**, *378*, No. 122191.

(36) Wilde, M.; Fukutani, K.; Ludwig, W.; Brandt, B.; Fischer, J. H.; Schauer, S.; Freund, H. J. Influence of carbon deposition on the hydrogen distribution in Pd nanoparticles and their reactivity in olefin hydrogenation. *Angew. Chem., Int. Ed.* **2008**, *47* (48), 9289–9293.

(37) Jansonius, R. P.; Schauer, P. A.; Dvorak, D. J.; MacLeod, B. P.; Fork, D. K.; Berlinguette, C. P. Strain influences the hydrogen evolution activity and absorption capacity of palladium. *Angew. Chem., Int. Ed.* **2020**, *59* (29), 12192–12198.

(38) Yue, L.; Song, W.; Zhang, L.; Luo, Y.; Wang, Y.; Li, T.; Ying, B.; Sun, S.; Zheng, D.; Liu, Q.; Farouk, A.; Hamdy, M. S.; Alfaifi, S.; Sun, X. Recent advance in heterogenous electrocatalysts for highly selective nitrite reduction to ammonia under ambient condition. *Small Structures* **2023**, *4* (11), No. 2300168.

(39) Pan, J.; Chen, N.; Cai, Q.; Pan, B. High N₂-selectivity of nitrite reduction by palladium-laden nanocomposite with self-sufficient electron donors. *Sci. Total Environ.* **2024**, *953*, No. 176126.

(40) Lim, J.; Chen, Y.; Cullen, D. A.; Lee, S. W.; Senftle, T. P.; Hatzell, M. C. PdCu electrocatalysts for selective nitrate and nitrite reduction to nitrogen. *ACS Catal.* **2023**, *13* (1), 87–98.

(41) Zhang, W.; Yao, Y.; Chen, Z.; Zhao, S.; Guo, F.; Zhang, L. Fluorine modification promoted water dissociation into atomic hydrogen on a copper electrode for efficient neutral nitrate reduction and ammonia recovery. *Environ. Sci. Technol.* **2024**, *58* (16), 7208–7216.

(42) Gao, W.; Xie, K.; Xie, J.; Wang, X.; Zhang, H.; Chen, S.; Wang, H.; Li, Z.; Li, C. Alloying of Cu with Ru enabling the relay catalysis for reduction of nitrate to ammonia. *Adv. Mater.* **2023**, *35* (19), No. 2202952.

(43) Liu, W.-S.; Chang, Y.-L.; Tan, C.-Y.; Tsai, C.-T.; Kuo, H.-C. Properties of N-type GaN thin film with Si-Ti codoping on a glass substrate. *Crystals* **2020**, *10* (7), 582.

(44) Jiang, K.; Wang, P.; Guo, S.; Zhang, X.; Shen, X.; Lu, G.; Su, D.; Huang, X. Ordered PdCu-based nanoparticles as bifunctional oxygen-reduction and ethanol-oxidation electrocatalysts. *Angew. Chem., Int. Ed.* **2016**, *128* (31), 9176–9181.

(45) Chen, S.; Brown, L.; Levendorf, M.; Cai, W.; Ju, S.; Edgeworth, J.; Li, X.; Magnuson, C. W.; Velamakanni, A.; Piner, R. D.; Kang, J.; Park, J.; Ruoff, R. S. Oxidation resistance of graphene-coated Cu and Cu/Ni alloy. *ACS Nano* **2011**, *5* (2), 1321–1327.

(46) Fang, J.-Y.; Zheng, Q.-Z.; Lou, Y.-Y.; Zhao, K.-M.; Hu, S.-N.; Li, G.; Akdim, O.; Huang, X.-Y.; Sun, S.-G. Ampere-level current density ammonia electrochemical synthesis using CuCo nanosheets simulating nitrite reductase bifunctional nature. *Nat. Commun.* **2022**, *13* (1), 7899.

(47) Li, Z.; Song, E.; Ren, R.; Zhao, W.; Li, T.; Liu, M.; Wu, Y. Pd-Pd/PdO as active sites on intercalated graphene oxide modified by diaminobenzene: fabrication, catalysis properties, synergistic effects, and catalytic mechanism. *RSC Adv.* **2022**, *12* (14), 8600–8610.

(48) Ren, S.; Gao, R.-T.; Yu, J.; Yang, Y.; Liu, X.; Wu, L.; Wang, L. Enhanced charge-carrier dynamics and efficient photoelectrochemical nitrate-to-ammonia conversion on antimony sulfide-based photocathodes. *Angew. Chem., Int. Ed.* **2024**, *63* (48), No. e202409693.

(49) Gao, Q.; Pillai, H. S.; Huang, Y.; Liu, S.; Mu, Q.; Han, X.; Yan, Z.; Zhou, H.; He, Q.; Xin, H.; Zhu, H. Breaking adsorption-energy scaling limitations of electrocatalytic nitrate reduction on intermetallic CuPd nanocubes by machine-learned insights. *Nat. Commun.* **2022**, *13* (1), 2338.

(50) Li, X.; Wang, C.; Yang, J.; Xu, Y.; Yang, Y.; Yu, J.; Delgado, J. J.; Martinson, N.; Sun, X.; Zheng, X.-S.; Huang, W.; Tang, J. PdCu nanoalloy decorated photocatalysts for efficient and selective oxidative coupling of methane in flow reactors. *Nat. Commun.* **2023**, *14* (1), 6343.

(51) Chen, C.; Zhu, X.; Wen, X.; Zhou, Y.; Zhou, L.; Li, H.; Tao, L.; Li, Q.; Du, S.; Liu, T.; Yan, D.; Xie, C.; Zou, Y.; Wang, Y.; Chen, R.; Huo, J.; Li, Y.; Cheng, J.; Su, H.; Zhao, X.; Cheng, W.; Liu, Q.; Lin, H.; Luo, J.; Chen, J.; Dong, M.; Cheng, K.; Li, C.; Wang, S. Coupling N₂ and CO₂ in H₂O to synthesize urea under ambient conditions. *Nat. Chem.* **2020**, *12* (8), 717–724.

(52) Dong, W. J.; Zhou, P.; Xiao, Y.; Navid, I. A.; Lee, J. L.; Mi, Z. Silver halide catalysts on GaN nanowires/Si heterojunction photocathodes for CO₂ reduction to syngas at high current density. *ACS Catal.* **2022**, *12* (4), 2671–2680.

(53) Zhou, B.; Zhan, G.; Yao, Y.; Zhang, W.; Zhao, S.; Quan, F.; Fang, C.; Shi, Y.; Huang, Y.; Jia, F.; Zhang, L. Renewable energy driven electroreduction nitrate to ammonia and in-situ ammonia recovery via a flow-through coupled device. *Water Res.* **2023**, *242*, No. 120256.

(54) Li, K.; Shi, Z.; Wang, L.; Wang, W.; Liu, Y.; Cheng, H.; Yang, Y.; Zhang, L. Efficient electrochemical NO reduction to NH₃ over metal-free g-C₃N₄ nanosheets and the role of interface microenvironment. *J. Hazard. Mater.* **2023**, *448*, No. 130890.

(55) Peng, O.; Hu, Q.; Zhou, X.; Zhang, R.; Du, Y.; Li, M.; Ma, L.; Xi, S.; Fu, W.; Xu, Z.; Cheng, C.; Chen, Z.; Loh, K. P. Swinging hydrogen evolution to nitrate reduction activity in molybdenum carbide by ruthenium doping. *ACS Catal.* **2022**, *12* (24), 15045–15055.

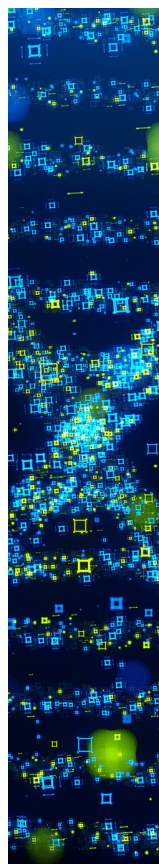
(56) Hao, R.; Song, Y.; Yang, L.; Guo, Y.; Wu, X.; Ma, Z.; Qian, Z.; Liu, F.; Wu, Z.; Wang, L. Electrochemical reduction of flue gas denitrification wastewater to ammonia using a dual-defective Cu₂O@Cu heterojunction electrode. *Environ. Sci. Technol.* **2024**, *58* (12), 5557–5566.

(57) Wu, Z.; Karamad, M.; Yong, X.; Huang, Q.; Cullen, D. A.; Zhu, P.; Xia, C.; Xiao, Q.; Shakouri, M.; Chen, F.; Kim, J. Y.; Xia, Y.; Heck, K.; Hu, Y.; Wong, M. S.; Li, Q.; Gates, I.; Siahrostami, S.; Wang, H. Electrochemical ammonia synthesis via nitrate reduction on Fe single atom catalyst. *Nat. Commun.* **2021**, *12* (1), 2870.

(58) Liang, J.; Li, Z.; Zhang, L.; He, X.; Luo, Y.; Zheng, D.; Wang, Y.; Li, T.; Yan, H.; Ying, B.; Sun, S.; Liu, Q.; Hamdy, M. S.; Tang, B.; Sun, X. Advances in ammonia electrosynthesis from ambient nitrate/nitrite reduction. *Chem.* **2023**, *9* (7), 1768–1827.

(59) Dong, W. J.; Ye, Z.; Tang, S.; Navid, I. A.; Xiao, Y.; Zhang, B.; Pan, Y.; Mi, Z. Concentrated solar light photoelectrochemical water splitting for stable and high-yield hydrogen production. *Adv. Sci.* **2024**, *11* (26), No. 2309548.

- (60) Liu, B.; Wang, T.; Wang, S.; Zhang, G.; Zhong, D.; Yuan, T.; Dong, H.; Wu, B.; Gong, J. Back-illuminated photoelectrochemical flow cell for efficient CO₂ reduction. *Nat. Commun.* **2022**, *13* (1), 7111.
- (61) Sun, S.; Dai, C.; Zhao, P.; Xi, S.; Ren, Y.; Tan, H. R.; Lim, P. C.; Lin, M.; Diao, C.; Zhang, D.; Wu, C.; Yu, A.; Koh, J. C. J.; Lieu, W. Y.; Seng, D. H. L.; Sun, L.; Li, Y.; Tan, T. L.; Zhang, J.; Xu, Z. J.; Seh, Z. W. Spin-related Cu-Co pair to increase electrochemical ammonia generation on high-entropy oxides. *Nat. Commun.* **2024**, *15* (1), 260.
- (62) Huang, Y.; He, C.; Cheng, C.; Han, S.; He, M.; Wang, Y.; Meng, N.; Zhang, B.; Lu, Q.; Yu, Y. Pulsed electroreduction of low-concentration nitrate to ammonia. *Nat. Commun.* **2023**, *14* (1), 7368.
- (63) Zhao, F.; Guo, Y.; Zhou, X.; Shi, W.; Yu, G. Materials for solar-powered water evaporation. *Nat. Rev. Mater.* **2020**, *5* (5), 388–401.
- (64) van Langevelde, P. H.; Katsounaros, I.; Koper, M. T. M. Electrocatalytic nitrate reduction for sustainable ammonia production. *Joule* **2021**, *5* (2), 290–294.
- (65) Dang, Q.; Zhang, W.; Liu, J.; Wang, L.; Wu, D.; Wang, D.; Lei, Z.; Tang, L. Bias-free driven ion assisted photoelectrochemical system for sustainable wastewater treatment. *Nat. Commun.* **2023**, *14* (1), 8413.
- (66) Guo, X.; Gao, R.-T.; Ren, S.; Nguyen, N. T.; Chen, H.; Wu, L.; Wang, L. Direct ammonia and dihydroxyacetone production in an unbiased photoelectrochemical cell. *Nat. Commun.* **2025**, *16* (1), 6220.
- (67) Huang, X.; Xie, S.; Sheng, B.; Xiao, B.; Chen, C.; Sheng, H.; Zhao, J. Air-level oxygen enables 100% selectivity in urea synthesis via photocatalytic C-N coupling of CO and ammonia. *Angew. Chem., Int. Ed.* **2025**, *64* (30), No. e202505630.
- (68) Ma, Y.; Guo, X.; Yuan, W.; Yang, P.; Zhang, Y.; Chen, W.; Cai, L.; Nicolosi, V.; Wang, W.; Chai, Y.; Qiu, B. Paired electrochemical synthesis of glycolic acid and ammonia from polyester and nitrate sewage. *Chem. Catal.* **2025**, *5* (6), No. 101336.
- (69) Dong, W. J.; Menzel, J. P.; Li, K.; Ye, Z.; Long, Z.; Navid, I. A.; Yang, K. R.; Xiao, Y.; Batista, V. S.; Mi, Z. Nitrate reduction to ammonia catalyzed by GaN/Si photoelectrodes with metal clusters. *Nat. Commun.* **2025**, *16* (1), 3383.
- (70) Pearson, R. G. Hard and soft acids and bases. *J. Am. Chem. Soc.* **1963**, *85* (22), 3533–3539.
- (71) Pearson, R. G. Absolute electronegativity and hardness: application to inorganic chemistry. *Inorg. Chem.* **1988**, *27* (4), 734–740.
- (72) Nørskov, J. K.; Rossmeisl, J.; Logadottir, A.; Lindqvist, L.; Kitchin, J. R.; Bligaard, T.; Jónsson, H. Origin of the overpotential for oxygen reduction at a fuel-cell cathode. *J. Phys. Chem. B* **2004**, *108* (46), 17886–17892.
- (73) Liu, J.-X.; Richards, D.; Singh, N.; Goldsmith, B. R. Activity and selectivity trends in electrocatalytic nitrate reduction on transition metals. *ACS Catal.* **2019**, *9* (8), 7052–7064.
- (74) Gupta, S.; Rivera, D. J.; Shaffer, M.; Chismar, A.; Muhich, C. Behavior of cupric single atom alloy catalysts for electrochemical nitrate reduction: an ab initio study. *ACS ES&T Engg.* **2024**, *4* (1), 166–175.
- (75) Zhu, X.; Fan, X.; Lin, H.; Li, S.; Zhai, Q.; Jiang, Y.; Chen, Y. Highly efficient electroenzymatic cascade reduction reaction for the conversion of nitrite to ammonia. *Adv. Energy Mater.* **2023**, *13* (20), No. 2300669.
- (76) Long, X.; Huang, F.; Zhong, T.; Zhao, H.; Li, P.; Fang, J.; Tian, S.; Shu, D.; He, C. One-step strategy to maximize single-atom catalyst utilization in nitrate reduction via bidirectional optimization of mass transfer and electron supply. *Environ. Sci. Technol.* **2025**, *59* (17), 8555–8567.



CAS BIOFINDER DISCOVERY PLATFORM™

STOP DIGGING THROUGH DATA —START MAKING DISCOVERIES

CAS BioFinder helps you find the
right biological insights in seconds

Start your search

CAS
A Division of the
American Chemical Society